The Epoch of Helium Reionization

Aaron Sokasian[1]

Tom Abel[2] and Lars Hernquist[3]
Department of Astronomy, Harvard University, Cambridge, MA 02138

ABSTRACT

We study the reionization of Helium II by quasars using a numerical approach that combines 3D radiative transfer calculations with cosmological hydrodynamical simulations. Sources producing the ionizing radiation are selected according to an empirical quasar luminosity function and are assigned luminosities according to their intrinsic masses. The free parameters associated with this procedure are: (1) a universal source lifetime, (2) a minimum mass cutoff, (3) a minimum luminosity cutoff, (4) a solid angle specifying the extent to which radiation is beamed, and (5) a tail-end spectral index for the radiative energy distribution of the sources. We present models in which these parameters are varied and examine characteristics of the resultant reionization process that distinguish the various cases. In addition, we extract artificial spectra from the simulations and quantify statistical properties of the spectral features in each model.

We find that the most important factor affecting the evolution of He II reionization is the cumulative number of ionizing photons that are produced by the sources. Comparisons between He II opacities measured observationally and those obtained by our analysis reveal that the available ranges in plausible values for the parameters provide enough leeway to provide a satisfactory match. However, one property common to all our calculations is that the epoch of Helium II reionization must have occurred at a redshift between $3 \lesssim z \lesssim 4$. If so, future observational programs will be able to directly trace the details of the ionization history of helium and probe the low density phase of the intergalactic medium during this phase of the evolution of the Universe.

Subject headings: radiative transfer – diffuse radiation – intergalactic medium – galaxies: quasars

---

[1]asokasia@cfa.harvard.edu

[2]hi@tomabel.com

[3]lars@cfa.harvard.edu

1.   INTRODUCTION

Space-based ultraviolet telescopes have made it possible to observe the Lyα transition of singly ionized helium (He II) along lines of sight to high-redshift quasars. The discovery of the "He II Gunn-Peterson effect" in Q0302-003 ($z = 3.285$) by Jakobsen et al. (1994) marked the beginning of He II Lyα studies. He II absorption in a second quasar, PKS 1935-692 ($z = 3.18$), was identified by Tytler (1995; see also Jakobsen 1996), while Davidsen et al. (1996) measured the He II opacity at a lower redshift of $z = 2.72$ towards the quasar HS 1700+6416 using the Hopkins Ultraviolet Telescope (HUT). These papers established the presence of He II absorption, albeit at low resolution, and indicated that the mean opacity increases with redshift. Later, Q0302-003 and HE 2347-4342 ($z = 2.885$) were observed individually by Hogan, Anderson & Rugers (1997) and Reimers et al. (1997) using the Goddard High Resolution Spectrograph (GHRS). Subsequently, Heap et al. (2000) and Smette et al. (2000) reported new HST/STIS spectra for Q0302-003 and HE 2347-4342, respectively. These observations had sufficient resolution to begin to resolve some of the features in the He II Lyα forest and also allowed them to to cross-correlate the data with the absorbers in the gaps of the hydrogen (H I) forest lines. In particular, the high quality of the STIS spectra reveals regions of high-opacity as well as ones of low opacity extending over several Mpc. Moreover, models of the spectra based on corresponding H I Lyα forests were presented to probe the hardness of the UV background, believed to emanate from the observed quasar population (e.g. Haardt & Madau 1996).

Due to its relatively higher optical depth compared to H I, He II serves as a better probe of diffuse gas residing in voids between galaxies (e.g. Croft et al. 1997). Resolving He II absorption features in quasar spectra can therefore reveal the presence of matter in large, low density regions, which, according to gravitational instability models of structure formation, harbor the bulk of the baryonic matter in the universe at high redshift (e.g. Davé et al. 2001; Croft et al. 2001). Interpreting observations of He II absorption will require comparisons with detailed models derived from cosmological hydrodynamical simulations which incorporate radiative transfer effects responsible for the photoionization of helium. In particular, it is of interest to develop an understanding of how individual sources act collectively in the reionization process.

In this paper we use the numerical approach described in Sokasian, Abel & Hernquist (2001, hereafter Paper I) to simulate the 3D reionization of He II by quasars. In particular, we explore the parameter space associated with the characteristics of the sources and study how they influence global properties of the reionization process. Comparisons with observational results are also made possible by extracting synthetic spectra from the simulations. Here our aim is twofold: to develop an understanding of the sensitivity of the

reionization process to source properties and to examine the predictions of the different models in light of recent observational results.

2. SIMULATING COSMOLOGICAL REIONIZATION

In general, a description of the evolution of ionization zones around cosmological sources requires a full solution to the radiative transfer equation. Such a solution would yield everywhere the monochromatic specific intensity of the radiation field in an expanding universe: $I_\nu \equiv I(t, \vec{x}, \hat{n}, \nu)$, where $\hat{n}$ is a unit vector along the direction of propagation of a ray with frequency ν. Presently, it is computationally impractical to acquire a complete, multi-dimensional solution for I_ν at the high resolution required for cosmological simulations. Our approach relies on a new algorithm which employs a simple jump condition to compute all radiative ionizations from a given source in a single step. This eliminates the need to repeatedly re-cast rays and calculate rates at every time step, thereby greatly speeding up the process. Moreover, our algorithm includes an approximate treatment of the diffuse component of the radiation field.

The approach we take is to approximately describe the evolution of the ionization state of the gas in a cosmological volume by iteratively calculating the net effect of ionizing sources at regularly spaced time intervals via a ray casting scheme. At the end of each interval, the effect of a diffuse ionizing background is accounted for by casting rays of ionizing radiation (according to a detailed prescription) inward from the sides of the simulation box. Density fields as well as information regarding sources will be specified from outputs at desired redshifts from a cosmological simulation. For simplicity, all sources are taken to have identical lifetimes. The details of the implementation of this method are discussed in Paper I.

Our approach requires a number of straightforward approximations to simplify the calculations; we review them here. First, our radiative transfer calculations are done on a uniform Cartesian grid whose scale L will always be much smaller than the horizon, $c/H(t)$, where c is the speed of light and $H(t)$ is the time dependent Hubble constant. This eliminates the need to include Doppler shifting of frequencies in line transfer calculations. Additionally, if the light crossing time L/c is much shorter than the ionization timescale, the time dependence of the intensities drop out as well. In the volumes we simulate, this will certainly be true and so we make this approximation as well. Next, we assume that the density field will experience negligible cosmological evolution during the lifetime of a single source. This requires us to consider only short-lived sources (at most a few $\times 10^7$ years). This assumption allows us to perform all our radiative calculations during a source's

lifetime in a static density field, greatly reducing the complexity of the algorithm.

Finally we ignore the dynamical consequences of thermal feedback into the gas from radiative ionization, enabling us to decouple our calculation of the radiation field from the hydrodynamical evolution of the gas. This allows us to use existing outputs from cosmological simulations to describe the evolving density field during the reionization process. In reality, photoheating introduces extra heat into the medium, and as ionization fronts (I-fronts) move from small scales to large scales, there is a corresponding transfer of power from small to large scales through nonlinear evolution. This effect is somewhat accounted for in the underlying cosmological simulation used in this paper which includes a uniform ionizing background capable of heating the gas. However, one also expects additional heating due to radiative transfer effects during the reionization process, and such uniform backgrounds cannot reproduce the observed increase in gas temperatures from the extra heating (Abel & Haehnelt 1999 and references therein). As a result, we expect minor systematic errors to be present in our solutions. However, the main purpose of this paper is to describe the general morphological evolution of the reionization process on large scales, which is insensitive to these systematic errors. In particular, recombination rates depend weakly on temperature and hence a proper accounting of photons is possible even if the temperatures are not computed precisely.

The cosmological simulation we will use in our analysis is based on a smoothed particle hydrodynamics (SPH) treatment, computed using the parallel tree-code GADGET developed by Springel, Yoshida & White (2001). The particular cosmology we examine is a ΛCDM model with $\Omega_b = 0.04$, $\Omega_{DM} = 0.26$, $\Omega_\Lambda = 0.70$, and $h = 0.67$ (see, e.g., Springel, White & Hernquist 2001). The simulation uses 224^3 SPH particles and 224^3 dark matter particles in a 67.0 Mpc/h comoving box, resulting in mass resolutions of 2.970×10^8 $M_\odot/h$ and 1.970×10^9 $M_\odot/h$ in the gas and dark matter components, respectively. The gas can cool radiatively to high overdensity (e.g. Katz, Weinberg & Hernquist 1996) and is photoionized by a diffuse radiation field which is assumed to be of the form advocated by Haardt & Madau (1996; see also, Davé et al. 1999). When sources are included in our treatment of helium reionization, the ionization state of the helium is recalculated, ignoring the diffuse background that was included in the hydrodynamical simulation (see Paper I for details).[4]

---

[4]We note that Springel & Hernquist (2001) have recently pointed out that for the specific hydrodynamical treatment we employ the amount of gas in cold, dense clumps is subject to some inaccuracy. In our calculations, however, these uncertainties are folded into our parameterization of the mass-to-light ratio and do not affect our ionization analysis.

3. SOURCE SELECTION AND MODELS

The full details of our source selection method are described in §4.2 of Paper I; here, we summarize the main steps and point out the modifications adopted for this paper. The basic procedure involves identifying dense clumps of gas particles in the cosmological simulation which represent plausible quasar locations, and adopting a prescription for selecting a subset of these objects as actual sources according to an empirical quasar luminosity function. The first task required is to store in descending order an array of redshifts, z_i, corresponding to intervals of one source lifetime, T_{life}. These redshifts will designate when sources turn on and off during the ionization calculation. Next, we loop over the cosmological simulation outputs, hereafter referred to as hydro outputs, to identify plausible sources. To identify quasars, we specify a maximum linking length corresponding to a group overdensity of roughly 200. Additionally, we specify a minimum mass, M_{min}, required for a group to be considered a source. For every possible source identified, the center of mass location and total gas mass of the group are recorded and stored in arrays.

Once a list of plausible sources for a given hydro output has been compiled, all identified groups (sources) are logarithmically binned by mass and a tally of the number of groups in each bin is made. The results can then be fitted to form an analytic representation of the mass function. Here we use a simple power-law of the form:

$$\frac{dN}{d\log M} = 10^{(a \log M + b)} \tag{1}$$

where dN is the number of groups with total gas masses between $\log M$ and $\log (M + dM)$, and a,b are fitted parameters. Our analytic representation is motivated by the general power-law nature of theoretical halo mass functions (see Press & Schechter 1974) and seems to produce reliable fits for the range of group masses found in our simulation volume. Due to the finite size of our volume, we inevitably fail to capture the most massive groups ($> 10 \times 10^{12}~M_\odot$) expected to exist on the exponential end of a theoretical galaxy mass function. However, the number of sources that would be selected off this end in our volume is less than unity on average, therefore we do not expect that their exclusion will significantly alter the results. Furthermore, the sources which are selected with our evolving mass-to-light ratio roughly reproduce the observed range of quasar luminosities at the corresponding redshifts, reassuring us that our cosmological volume is sufficiently large enough to properly sample a representative subset of group masses.

Our next step is to define a selection criterion which will determine a realistic subset of sources that will actually be activated during the calculation of the radiation field. In particular, we would like to select sources according to the observed quasar luminosity function $\phi(L, z)$ (LF). Here, $\phi(L, z)~dL$ is the number of quasars per unit comoving volume

at redshift z, with intrinsic luminosities between L and $L + dL$. Given the observational data, the inferred luminosity function will depend upon the assumed cosmology and quasar spectra. In our simulations, we will adopt the double-power-law model presented by Boyle et al. (1988) using the open-universe fitting formulae from Pei (1995) for the B-band (4400 Å rest-wavelength) LF of observed quasars, with a rescaling of luminosities and volume elements for our ΛCDM cosmology. The parametric form of the double power-law LF can be written as

$$\phi(L, z) = \frac{\Phi_\star / L_z}{(L/L_z)^{\beta_1} + (L/L_z)^{\beta_2}}, \tag{2}$$

where the break luminosity, L_z, evolves with redshift according to:

$$L_z = L_\star (1 + z)^{\alpha - 1} \exp[-(z - z_\star)^2 / 2\sigma_\star^2]. \tag{3}$$

In this model, the abundance of quasars peaks at $z_\star$ with a characteristic dispersion of $\sigma_\star$. The redshift factor $(1 + z)^{\alpha - 1}$ represents the explicit dependence on the spectral index α where a UV spectrum, $f(\nu) \propto \nu^{-\alpha}$, has been assumed. The values of the fitting parameters are $z_\star = 2.77$, $\sigma_\star = 0.91$, $\beta_1 = 1.83$, $\beta_2 = 3.70$, $log(\phi_\star / \mathrm{Gpc}^{-3}) = 2.37$, and $log(L_\star / L_\odot) = 13.42$ for an open-universe cosmology with $h = 0.50$, $q_o = 0.1$, and $\alpha = 1.0$. We use the above values and convert the LF to our ΛCDM cosmology by rescaling the luminosity and volume element for each redshift of interest. Our conversion of the LF ignores any spectral-dependent k-corrections which are thought to be small assuming an $\alpha = 1.0$ power law for the quasars (Haiman & Loeb 1998). It is important to point out that this model predicts that a large fraction of the luminosity at $z > 2$ arises from quasars that have not yet been observed. With a fit to the LF which goes as $\phi(L) \propto L^{-1.83}$ at the faint end, the emissivity, $\int \phi(L, z) \, L \, dL$ (in ergs s^{-1} Hz^{-1} cm^{-3}), converges only as $L^{0.17}$, and it becomes apparent that a large portion of the total emissivity will arise from this regime. Nevertheless, the extrapolation of the LF to fainter quasars seems to be reasonable based on the analysis of Haardt & Madau (1996) where they use the above LF and a realistic form for quasar spectra to calculate the intensity of the ionizing background, J. Using the cosmological radiative transfer equation for diffuse radiation (e.g. Peebles 1993),

$$\left(\frac{\partial}{\partial t} - \nu \frac{\dot{a}}{a} \frac{\partial}{\partial \nu} \right) J = -3 \frac{\dot{a}}{a} J - c\kappa J + \frac{c}{4\pi} \epsilon, \tag{4}$$

where a is the scale factor, κ is the continuum absorption coefficient per unit length along the line of sight, and ϵ is the proper space-averaged volume emissivity, Haardt & Madau include the effects of absorption and emission by intervening clouds to calculate the evolution of J. They show that $J_{912 \, \text{Å}}$ increases from $\approx 10^{-23}$ ergs s^{-1} cm^{-2} sr^{-1} Hz^{-1} at the present epoch to $\approx 5 \times 10^{-22}$ ergs s^{-1} cm^{-2} sr^{-1} Hz^{-1} at $z = 2.5$. This result is

consistent with high-resolution studies of the proximity effect which give $J_{912\ \text{Å}} \approx 5 \times 10^{-22}$ obtained for a redshift range $z = 1.7 - 4.1$ (Giallongo et al. 1996) and $J_{912\ \text{Å}} \approx 10 \times 10^{-22}$ (Cooke et al. 1997) for a similar redshift range. It is furthermore consistent with limits imposed by the opacity of the Lyman alpha forest at both high (e.g. Rauch et al. 1997) and low (e.g. Davé et al. 1999) redshifts.

While our choice for the quasar LF appears reasonable, one must bear in mind that it is based on empirical results in only the B-band. It is therefore possible that there may be subtle selection effects which shroud the underlying form of the LF. In fact, the results of a soft X-ray $ROSAT$ survey of active galactic nuclei (AGN) by Miyaji, Hasinger, & Schmidt (2000) suggest that the quasar LF differs from the one presented above. Unlike optically selected quasars, the evolution of the $ROSAT$-selected quasars do not show evidence for a decrease in number density at redshift higher than 3. In particular, the X-ray selected AGNs from the survey conducted by Miyaji, Hasinger,& Schmidt with Log $L_x > 44.5$ have a space density seven times higher than optically selected quasars from the survey conducted by Schmidt et al. (1995). Although the statistical significance of the difference is marginal (2σ), the discrepancies may be indicative of different formation epochs for low and high mass black holes in the centers of the sources.

To be able to utilize the LF in our selection process, we will first need to prescribe some way of assigning luminosities to our list of plausible sources. This will involve adopting a mass-to-light ratio based on the minimum B-band luminosity (L_{min}) and a minimum mass for sources at every epoch. In Paper I, we considered only the bright sources and therefore adopted a mass-to-light ratio based on a constant L_{min} and M_{min}. Here we will consider the entire range of sources responsible for the emissivity implied by the luminosity function. This requires us to adopt a minimum luminosity which scales with z as the break luminosity L_z and is chosen to correspond to a set value $L_{min,o}$ at $z = 0$. We assume that the minimum mass required to form the quasar remains constant with redshift so that our expression for the mass-to-light ratio becomes,

$$\xi(z_i) = \frac{M_{min}}{L_{min,o}}\exp\left[\frac{z_i^2 - 2z_i z_\star}{2\sigma_\star^2}\right]. \tag{5}$$

The assumption that M_{min} is constant in time is motivated by the idea that there is a certain mass threshold required for the emission mechanism in quasars to operate. Both M_{min} and $L_{min,o}$ will act as free parameters in our analysis.

The selection process is initiated by first determining the number of sources expected at each redshift z_i,

$$N_e(z_i) = V_{box} \int_{L_{min}(z_i)}^{\infty} \phi(L_B, z_i)\ dL_B. \tag{6}$$

where V_{box} represents the comoving volume of the simulation and $L_{min}(z_i) = L_{min,o}$ $\exp[\frac{-z_i^2 + 2z_i z_\star}{2\sigma_\star^2}]$. N_e will thus designate the total number of sources chosen at redshift z_i. To convert N_e to an integer in an impartial manner, a random number between 0 and 1 is generated and compared to the fractional component of N_e. If the fractional component is larger than the generated number, N_e is rounded up to the nearest integer, else N_e is rounded down.

Next, we loop over every plausible source to determine whether it will be chosen. Our selection criterion will consist of assigning a random number between 0 and 1 to the candidate source of mass M and selecting it if the assigned value matches or falls below the value of a some probability function $P(M)$. To ensure that we match the quasar luminosity function, we define the probability function to be:

$$P(M) = \left(\frac{dN}{dM}\right)_{LF} \left(\frac{dN}{dM}\right)_{Hydro}^{-1}, \tag{7}$$

where $(dN/dM)_{LF}$ is the expected source mass function for a simulation box with comoving volume, V_{box}, as derived from the luminosity function:

$$\left(\frac{dN}{dM}\right)_{LF} = \xi(z_i)^{-1} \phi(M/\xi(z_i), z_i) V_{box}, \tag{8}$$

and $(dN/dM)_{Hydro}$ is just our analytic representation of the mass function obtained from the actual hydro simulation now rewritten as:

$$\left(\frac{dN}{dM}\right)_{Hydro} = M^{-1} 10^{(a \log M + b)}. \tag{9}$$

The loop is terminated when exactly N_e sources have been selected. If the number selected falls short of N_e after one run through the list of plausible sources, the list is reordered randomly and source selection is continued from the beginning of the list. In this manner, a list of sources is compiled for every redshift step of the simulation, z_i, with plausible source lists and mass functions being updated near every hydro output redshift.

Once a source with mass, M, has been selected, it is assigned a B-band luminosity, $L_B = M/\xi(z_i)$ (in ergs s^{-1}). This luminosity along with an assumed spectral form, is then used to compute the quantity of He II ionizing flux that will be generated while the source is active. In this paper, we shall assume for all sources, a multi-power-law form for the spectral energy distribution (SED),

$$L(\nu) \propto \begin{cases} \nu^{-0.3} & (2500 \text{ Å} < \lambda < 4400 \text{ Å}); \\ \nu^{-0.8} & (1050 \text{ Å} < \lambda < 2500 \text{ Å}); \\ \nu^{-\alpha_s} & (\lambda < 1050 \text{ Å}), \end{cases} \tag{10}$$

where a choice of $\alpha_s = 1.8$ gives the SED proposed by Madau, Haardt, & Rees (1999) based on the rest-frame optical and UV spectra of Francis et al. (1991), Sargent, Steidel, & Boksenberg (1989), and the EUV spectra of radio-quiet quasars (Zheng et al. 1998). We also allow for the possibility of bipolar beamed radiation fields by introducing the parameter, β, which specifies the beaming angle of the radiation from the sources. At the end of the entire source selection process, we will have recorded a list of source locations and ionization rates for every redshift step of the simulation and we can initiate the radiative transfer calculations (see Paper I). In selecting the sources and computing their intensities we have introduced five free parameters associated with source characteristics, they are: (1) a universal source lifetime, T_{life}, (2) a minimum mass, M_{min}, (3) a minimum luminosity at $z = 0$, $L_{min,o}$, (4) an angle specifying the beaming of the bi-polar radiation, β, and (5) a tail-end spectral index, α_s, in the regime $\lambda < 1050$ Å.

In this paper we compute and analyze 6 models with different sets of values for the free parameters. Table 1 lists the choices for each model. Model 1 will represent our fiducial case. In this model, the value for the source lifetime simply reflects a reasonable choice based on the quasar light curve derived by Haiman & Loeb (1998) for a similar cosmology and luminosity function. Our choice for $L_{min,o}$ in the model is based on the results of Cheng et al. (1985) who show that the LF of Seyfert galaxies (which are well correlated with that of optically selected quasars at $M_B = -23$) shows some evidence of leveling off by $M_B \simeq -18.5$ or $L_{min} \simeq 6.44 \times 10^9 \ L_{B,\odot}$ at $z = 0$. The value of M_{min} is then chosen such that the B-band emissivity from the selected sources matches the expected emissivity derived from the LF. Given our value for $L_{min,o}$, we find $M_{min} = 1.42 \times 10^{10} \ M_\odot$ is able to match the derived B-band emissivity to within a few percent at z=3 for this particular case. This value seems reasonable given the assumption that the sources are galaxy type objects acting as hosts for quasars. It is also important to note that the underlying cosmological simulation used in this paper provides an acceptable level of resolution at this mass limit and thereby provides us with a realistic mass function for the source selection process. Furthermore, we are able to reproduce roughly the same range of observed B-band luminosities for the brightest quasars in the survey conducted by Warren, Hewett & Osmer (1994). Consequently, our ability to properly match the high end of the luminosity function with our most massive groups ensures that our volume is large enough to properly sample the range of source masses. The next parameter in the model describes the way sources beam their radiation. Here in our fiducial model, we choose our sources to radiate their flux isotropically by setting the beaming angle of the bi-polar radiation field to $\beta = \pi$. And for the final parameter, the tail-end spectral index, we choose the value $\alpha = 1.8$, making the SED in this model identical to the one proposed by Madau, Haardt, & Rees (1999).

Model 2 is identical to model 1 except for the anisotropic casting of the radiation

identified by a beaming angle of $\pi/2$. In models 3 and 4, we retain all the values as in our our fiducial model (model 1) but vary the source lifetimes by a factor of 2 in each direction. In model 5, in an attempt to examine the effect of a reduced level of ionizing emissivity, $L_{min,o}$ is increased by a factor 4 and the spectral index is set to $\alpha = 2$. For model 6, we also reduce the expected ionizing emissivity, however we do so only by steepening the spectral index by itself to the value of $\alpha = 2.3$.

It is important to point out that even the brightest and most long lived sources arising in any of the models have ionizing intensities which limit them to spheres of influence that are much smaller than the size of the simulation box. As a result, our simulation box is sufficiently large to statistically examine the epoch when sources are just turning on. When the medium has become mostly ionized, we utilize enough rays to properly track the contribution of ionizing photons from each source to the diffuse component of the radiation field.

The six models described above each predict a unique set of sources which are responsible for the ionization of the IGM. To compare the differences, we ran each model on the same cosmologically evolving density field (see §4.3 of Paper I for details regarding the evolution of the grids) from $z \simeq 5.7$ to $z \simeq 2.7$. We discuss the results from these models in the next section.

4.   RESULTS

In this section, we discuss the outcome of the simulations and present an analysis geared towards identifying and differentiating global characteristics of the models. In addition, we will describe our method for extracting artificial spectra from the outputs and present a comprehensive statistical study of spectral features extracted from each model.

4.1.   Ionizing photons

In Figure 1 we show the number of He II ionizing photons per comoving volume released from the sources as function of redshift for each model. The solid histogram in each plot specifies the number of ionizing photons released per unit volume at each redshift bin and the dashed curve represents the corresponding cumulative value. The widths of the bins in each histogram represent the source lifetime in the model. Models 1, 3, and 4, differ only in the source lifetime parameter; consequently, the total number of sources invoked in these models is in direct proportion to the ratios of their source lifetimes: 2:4:1,

respectively. Model 2 has a greater abundance of sources relative to model 1 due to the larger number of sources needed to match the implied number density from the observed LF, assuming the radiation from the sources is being beamed into two symmetric polar cones of width β radians. In particular, assuming the polar directions for the radiation are randomly distributed (a condition which we have implemented), the number of expected sources is proportional to $(1 - \cos \frac{\beta}{2})^{-1}$. This amounts to an excess factor of 3.41 for the number of sources in model 2 relative to model 1. Note, however, that the number of ionizing photons released in both models is the same. In fact, this is true for models 1-4 where we have matched the values for the parameters M_{min}, $L_{min,o}$ and α_s. In models 5 and 6, the new choices for $L_{min,o}$ and α_s lead to a relative paucity in the number of ionizing photons compared to models 1-4 (see Figure 1). In particular, the cumulative number of ionizing photons released in the 10^6 Mpc^3 comoving volume by $z \simeq 2.75$ in models 1-4 was 4.08×10^{72} compared to 1.34×10^{72} and 1.47×10^{72} for models 5 and 6 respectively. It is thus clear that the choices for $L_{min,o}$ and α_s have a substantial influence on the amount of ionizing radiation that is emitted from the sources. This is also true for the parameter M_{min}, but we have chosen to hold it fixed in the models considered in this paper.

To illustrate how the results in Figure 1 depend on each parameter, in Figure 2 we compare the cumulative number of ionizing photons that are released per unit comoving volume as a function of redshift between models as the parameters are varied separately. It is evident that there is a strong dependence on each of the parameters and this will be an important point to consider when discussing the evolution of the reionization process and its sensitivity to the cumulative influence of ionizing radiation.

4.2. Global ionization fractions

We now discuss global properties of the ionization state of the volume for the various models considered. In Figures 3a and 3b we show how the ionized mass and volume fraction, respectively, evolve with redshift. In all our models, He II is mostly fully ionized by $z \simeq 3.3$, a result which is in accord with observations (Jakobsen et al. 1994; Davidsen, Kriss, & Zheng 1996; Hogan, Anderson, & Rugers 1997; Reimers et al. 1997; Anderson et al. 1999; Heap et al. 2000; Smette et al. 2000). The evolution to a completely ionized state is quite similar for all the models with the exception of models 5 and 6 where the lower emissivities lead to a more gradual rise in the ionized fractions. Nevertheless, the entire volume is essentially fully ionized by $z \approx 3.3 - 3.8$ in all our models. Thus, we predict that the opacity of the He II Lyman alpha forest should increase rapidly for $z > 3$ and that the redshift evolution of this opacity will contain information that can be used to discriminate

between models like those considered here (i.e. models 5 & 6 versus models 1-4).

It is also quite evident from Figures 3a and 3b, that whereas the volume is essentially fully ionized by $z \sim 3.3$, this is not necessarily true of the mass. This is a consequence of extremely overdense cells with large clumping factors which quickly recombine after they have been ionized. In models 5 and 6, lower photoionization rates make it even harder to keep these cells ionized. Due to their large overdensities (factors of 10^3 or more) it takes relatively few such cells to substantially lower the ionized mass fraction. These cells will not, however, strongly influence the mean opacity of the He II Lyman alpha forest, which directly measures the volume fraction ionized.

In Figure 3c, we plot the ratio of the ionized mass fraction to the ionized volume fraction as a function of redshift for each model. Here, we can more clearly see how the ionized mass fraction dominates the corresponding volume fraction at high redshifts. This is consistent with the idea that at earlier times, when the medium is mostly neutral, the densest and most compact regions immediately surrounding the sources are the first to become ionized. However, with time, the ionization fronts expand into the less dense but more voluminous voids, thereby decreasing the ratio shown in Figure 3c and eventually leveling it off to a value slightly less than unity.

One may conjecture that the epoch of overlap, when intervening patches of He II no longer obscure the field of view from any source and the universe becomes transparent on a much larger scale than during the previous stage, may be reached as the ionized volume fraction approaches unity. Testing this idea requires additional analysis into the evolution of the ionizing background. Namely, once the volume is sufficiently ionized so that every sources can *see* every other source, the ionizing intensity of the background is expected to rise sharply as the contributions from different sources combine. Such an effect was reported by Gnedin (2000), whose simulations of cosmological reionization by stellar sources predict an overlap epoch in hydrogen that is characterized by a sharp rise in the level of the ionizing background and in the photon mean free path.

To see if we predict a similar rise, we have plotted in Figure 4 the number of ionizing photons per helium atom available in the diffuse component of the radiation field as function redshift for model 1 (models 2-4 demonstrated very similar results and are not shown). Here we do indeed see a similar steep rise in the background with decreasing redshift starting at $z \simeq 3.7$. From Figure 3b, we note that this is right around the time when the corresponding volume fraction for model 1 has reached unity. There is a rise of nearly a factor of 100 in the background intensity between $3.2 \leq z \leq 3.7$ (corresponding to the region between the dashed lines) before leveling off. It thus seems reasonable to label this short era as the epoch of overlap immediately preceding complete reionization, which in this case would

be reached at $z \simeq 3.2$. In the case of models 5 and 6, the volume fraction does not reach unity until $z \sim 3$, near the redshift where we stop our calculations. We thus would expect a similar type of rise in the corresponding backgrounds in these models as well. However, we speculate whether the rise would be as dramatic as the one seen in model 1 since in models 5 and 6 the epoch of overlap occurs right around the time when the LF predicts a steep downturn in the ionizing emissivity of the contributing sources.

4.3.   Clumping characteristics within ionized regions

To track how I-fronts expand into the densest structures, we track the evolution of the mean clumping factor in ionized regions. In Figure 5, we plot the evolution of the ratio of the clumping factor of the ionized gas to the clumping factor of the entire volume as a function of redshift for each model. Clumping factors are computed on a fixed mesh of limited resolution based on an underlying smoothed density field. As such, one should be careful not to attach physical significance to the actual values, but rather view them as a tool to differentiate between the morphological evolution in each model. Our condition for considering a cell to be *ionized* is that the gas within is ionized by at least 90% in mass. An immediate consequence of this is that models 5 and 6, which lack the emissivity to retain high ionization fractions in the densest cells, have much lower clumping factors within their *ionized* regions. In models 1–4, the systematic increase in the clumping factors once most of the volume has been ionized ($z \lesssim 3.3$) is consistent with the interpretation presented by Miralda-Escudé, Haehnelt, & Rees (2000) in which they argue that in the post-reionization stage, the densest clouds and filaments (which dominate the overall clumping factor) gradually become ionized as the mean ionizing intensity increases. Nevertheless, a general feature among all the models is the tendency of the clumping factor of the ionized regions to remain well below the levels of the overall clumping factor for the entire volume, even at $z \simeq 2.8$. This feature is a consequence of a small number of highly overdense, mostly neutral cells which dominate the overall clumping factor. The difficulty in ionizing these cells is also reflected in the discrepancy between the mass and volume ionization fractions in Figure 3.

4.4.   Photoionization rates

In the left panel of Figure 6, we plot the volume-weighted global He II photoionization rate as a function of redshift for each model. Global rates were obtained at discrete redshifts by averaging over the rates in each cell of the corresponding grid (see §3.3 of Paper I for

a description on how photoionization rates are computed). Note that the rates begin to level off at $z \sim 3$, consistent with the LF used in this paper. The plot also shows why photoionization proceeds more slowly in models 5 and 6 compared with the others. In addition, the radiation field in model 3, although not as weak as those in models 5 and 6, is somewhat weaker than that in models 1, 2, and 4.

In the right panel of Figure 6, we plot the ratio of the dispersion in the photoionization rates to the corresponding photoionization rate. The dispersion in the rates is remarkably high and explicitly demonstrates the non-uniform nature of the radiation field from local sources. The particularly large amplitude of the dispersion in models 5 and 6 relative to the others is a natural consequence of the higher opacity in these models which inhibits uniformity in the photoionization rate. It is also interesting to point out the somewhat larger dispersion seen in models 2 and 3 relative to models 1 and 4. This is most likely due to the large number of sources in these models which can lead to a highly irregular radiation field. In the case of model 2, there is the additional ingredient that the ionizing flux is released anisotropically ($\beta = \pi/2$) from the sources. The cone shaped beaming of the radiation in this model only enhances the other factors responsible for large dispersions in the photoionization rates.

4.5. Spectral analysis

It is now believed that absorption by diffuse, cosmologically distributed gas is responsible for the hydrogen Lyman alpha forest (e.g. Cen et al. 1994; Zhang et al. 1995; Hernquist et al. 1996). Similarly, Lyα absorption by He II along a line of sight (LOS) to a distant quasar probes gas in the intervening IGM at even lower overdensities (Croft et al. 1997).

To relate our models to observations of quasars, we extract artificial Lyα absorption spectra from the simulation outputs and then derive statistical properties of the spectral features seen in each model. Of particular importance is the He II mean optical depth, which we compare to observational results in §4.5.4.

We extract artificial Lyα absorption spectra using the particle information in the SPH simulation coupled with the time-dependent ionization fractions from the radiative transfer calculations. For each model, we generate 500 spectra along randomly selected lines of sight between $z \simeq 2.8 - 3.6$. Our procedure is similar to that contained in the TIPSY software package (Katz & Quinn 1995), but does not require that a LOS be perpendicular to a box face in the simulation volume. Each LOS has a unique and arbitrary direction

relative to the box coordinate system and wraps through the simulation volume repeatedly via periodic boundaries. Our method also interpolates the hydrodynamic quantities and ionization state variables between consecutive data dumps and hence can construct spectra of any length in redshift space.

Using the smoothing kernels of the SPH particles, gas densities and temperatures are computed along a LOS at intervals corresponding to a resolution of at least $\lambda = 0.03$ Å. The component of the peculiar velocity of the gas in the direction of the LOS is also computed at each point. Once all physical quantities have been gathered, Voigt profiles are fitted to each spectrum by interpolating between the corresponding line-absorption coefficients provided in Harris (1948). It is important to point out that in computing the line profiles we use a minimum gas temperature of 2.0×10^4 K as a correction to the SPH temperatures which exclude the extra heating introduced by radiative transfer effects (see Abel and Haehnelt, 1999).

Information related to the hydrodynamical state of the particles is updated at SPH output redshifts of $z = 3.59$, 3.47, 3.36, 3.24, 3.14, 3.03, 2.94, 2.84 and 2.75. Ionization fractions, which evolve on shorter timescales, are updated after each source lifetime by mapping grid outputs from the radiative transfer calculations onto the particles. Moreover, the arrival times of the I-fronts (see section §3.1.3 of Paper I) in each grid are used to discriminately update the fractions along the LOS within a single source lifetime interval.

We have tested our technique for extracting physical properties as a function of redshift against the results of the TIPSY software package for lines of sight perpendicular to box faces of the simulation volume and find excellent agreement in all cases.

Figure 7 shows a sample spectrum from model 1 along a LOS that spans $z \simeq 2.8 - 3.6$ together with corresponding plots of the singly ionized fraction and gas density as a function of redshift. The rise of the neutral fraction with redshift and the corresponding decrement in transmission is quite evident from the panels in Figure 7.

In Figure 8, we plot transmission spectra for the different models along a particular LOS. In models 1, 2 and 4, where most of the IGM is in a highly ionized state, one can easily recognize similarities in the spectral features due to the underlying density and velocity structures. Models 3, 5 and 6 are different in this respect, because the relatively large neutral fractions in the gas lead to high optical depths which shroud the underlying structures. This is especially true for models 5 and 6 where large sections of the spectra near the red end are completely opaque due to weak ionizing intensities.

The dashed vertical line through the panels in Figure 8 at 1307 Å is a crude attempt to separate the spectra into two regimes that represent a high (*left*) and low (*right*) level

of ionization in the gas based on the general features in models 1-4. We use this dividing point in our forthcoming analysis of the spectral features in an effort to probe the evolution of the ionization state of the IGM using absorption spectra.

We note that the spectra extracted from models 5 and 6, where the volume fraction of ionized He II starts to drop rapidly for $z > 3.3$ (see Figure 3), exhibit extended wavelength intervals with virtually no transmission. A similar behavior is seen in models 1-4 for $z > 3.8$. Thus, our analysis predicts that future observations of the He II Lyman alpha forest in quasar spectra should show a dramatic drop in transmission during the epoch of He II reionization, between $z \sim 3.3 - 3.8$.

4.5.1. Intersections versus transmittance

In this section we consider a more comprehensive analysis tool that utilizes information from the spectra at all transmission levels. The analysis involves tracking the number of intersections that occur through the spectra as a function of transmittance. Figure 9 shows the results of the analysis for each model averaged over 500 lines of sight, again focusing on two separate spectral segments. In both segments we see dramatically different results between models. In segment B (*left*), which represents the high redshift component of the spectral range, we note that the curves from models 1, 2 and 4 appear to posses local maxima near the 30% transmittance level. The curves from models 3, 5 and 6 exhibit no such peak and instead possess exponential type forms. In segment A (*right*) we notice that the curves from model 1, 2 and 4 have now converged to a skewed form which peaks near a transmittance of 80%. Furthermore, model 3 appears to have developed a local maximum with a form similar to the curves seen in models 1, 2 and 4 from segment B. Interestingly, models 5 and 6 appear to be following in model 3's footsteps.

A strong evolution of spectral features is clearly seen in these plots. In particular, in the models where the IGM has not yet become thoroughly ionized, the intersections decrease asymptotically with transmittance. However, as the IGM is gradually ionized to higher degrees, the intersections appear to peak first at low transmittance levels then move towards higher levels. Eventually, the curves converge to a form that rises linearly with transmittance, peaks, and then asymptotically falls off near a transmittance of 100%.

It is clear from this discussion that even as simple a diagnostic tool as that shown in Figure 9 can strongly discriminate between models and their rates of evolution. For example, consider model 3 whose spectrum in segment A visually looks very much like the spectra from models 1, 2 and 4 (see Figure 8), yet in the right-hand panel of Figure 9,

one can clearly see the disparity. On this basis, we anticipate that similar tools applied to observations of the He II Lyman alpha forest forest should constrain the nature of the sources responsible for the hard component of the ionizing radiation field.

4.5.2. Probability distribution function of transmittance

We next consider the probability distribution function of the transmittance (TPDF) as another tool to study the properties of the absorption spectra. The TPDF for each model was measured by averaging over 500 spectra, with all pixels weighted equally. We use 30 bins of equal width between the 0 and 1 transmission level. Figure 10 shows the TPDF (*left*) and the cumulative TPDF *right* for each model. Again, there is an obvious contrast between the models. The TPDF for models 1, 2 and 4 exhibit strong peaks near a transmittance of 0.9 while models 5 and 6 clearly do not; Model 3, however, seems to again reflect an intermediate case, possessing a peak near 0.9, but not at an amplitude similar to those of models 1, 2 and 4. The sharp rise near zero transmittance seen in all the models reflects the presence of trough-like features in the spectra. Naturally, as the IGM becomes more transparent, such features become less prevalent. This attrition is made evident from the relatively small amplitudes seen in the cumulative TPDF near zero transmittance for models 1, 2, and 4, all of which harbor gas with relatively high ionization fractions.

The form of the TPDF implied by our models is reminiscent of the transmitted flux PDFs (TFPDF) measured for the hydrogen Lyman alpha forest by McDonald et al. (2000). In particular, they use a sample of eight quasars observed at high redshift to determine the TFPDF in three redshift bins centered on $z =$ 2.41, 3.00, and 3.89. In their highest redshift bin ($z =$ 3.89), the TFPDF measured by McDonald et al. resembles the TPDF from our model 3. At their lower redshifts ($z =$ 3.0, 2.41), their TFPDF's begin to resemble the results from our models 1, 2 and 4.

4.5.3. Redshift evolution of the mean optical depth

Figure 11 shows the redshift evolution of the effective mean optical depth for He II absorption, which we define as $\bar{\tau}_{\mathrm{He\ II}} \equiv -\log_e \langle T \rangle$, where T is the transmittance. The average is performed over 500 lines of sight within 35 wavelength bins of width $\Delta\lambda = 6.57$ Å. Hatched regions represent the optical depth derived from the simulations at the 95% confidence level with the dashed lines indicating mean values. For comparison, we also plot the opacities measured at different redshifts in the spectra of Q 0302-003 (Heap et al.

2000), PKS 1935-692 (Anderson et al. 1999, reported values come from Smette et al. 2000 who perform an optimal reduction of the whole data set), and HE 2347-4342 (Smette et al. 2000). Horizontal lines through the data points represent the redshift range over which the opacity was averaged. Data points with no horizontal lines represent measurements made at specific wavelengths and should be assigned less weight as they do not represent mean opacities.

For models 1, 2, and 4, it appears that most of the measured opacities are much larger than predicted by our analysis. Model 3 does better, though falls short of the majority of data points near $z \simeq 2.85$. On the other hand, models 5 and 6 exhibit larger optical depths, and model 5, in particular, appears to be in reasonable agreement with the data. It is important to point out, however, that the observed values are likely subject to a great deal of statistical variance. In particular, the hatched regions in Figure 11 represent averages over 500 lines of sight, whereas the observational data stem from only 3 lines of sight. One therefore needs to be careful when making judgments regarding the *best-fit* model. Nevertheless, such comparisons provide an important point of reference upon which to base claims regarding the nature of the sources. We shall discuss such conclusions in the following section.

5. DEPENDANCE ON CLUMPING AND TEMPERATURE OF THE IGM

Both the temperature and clumping factor of the IGM play an important role in the evolution of the reionization process by influencing the rate at which recombinations take place in ionized regions. The analysis presented in this paper uses approximate techniques to set the values of these parameters; it is therefore necessary to explore the associated parameter space to acquire some intuition for their potential impact on the reionization process.

In Figure 12, we compare ionized mass (*left*) and volume (*right*) fractions between our fiducial model 1 and two additional models, model 1a and 1b, which are identical to model 1 except for temperatures and clumping factors. In model 1a, the temperature of the ionized gas was set to 7000 K as opposed to 2.0×10^4 K as in model 1. In model 1b, all the information regarding the clustering of particles was disregarded by setting cell clumping factors to unity. We note that these are extreme limiting cases to consider, but they do indicate potential sources of error in our analysis.

In the case of model 1a, the slight drop in the ionized fractions reflects the greater difficulty involved in ionizing a relatively cooler medium where recombinations are more

prevalent. This dependence of the optical depth on the temperature of the gas is also well known in the case of the hydrogen Lyman alpha forest (see Machacek, et al. 2000 for a detailed discussion and references). Conversely, in model 1b, recombinations are less prevalent than in model 1 due to the adoption of a uniform distribution of the gas in each cell ($C_f = 1$) and as a result ionization fractions are consistently larger at each redshift. More specifically, at $z = 3$, models 1a and 1b produce respectively a -3.3% and 4.7% difference in the ionized mass fraction compared to model 1.

A comparison of the mean optical depths between these cases is shown in Figure 13. The results were again computed using a statistical pool of 500 lines of sight. The relative opacities seen in model 1a and 1b are consistent with the discussion above. The shift in temperatures between models 1 and 1a appears to have a more significant impact on the mean optical depth than does ignoring the clumping of gas within cells. However, it does not appear that temperature variations can reconcile the deficit between the observed values of the mean optical depth and those inferred from our analysis for this particular model.

6.   SUMMARY AND CONCLUSIONS

The most important factor determining the reionization history of He II is the cumulative number of ionizing photons that are produced by the sources. Given a specific form for the LF, ionizing emissivities are ultimately determined by intrinsic source characteristics such as their minimum luminosity and spectral energy distribution. In the analysis presented here, a numerical method designed to follow the inhomogeneous reionization of a cosmological volume by a set of point sources (quasars) was used to explore a small portion of the parameter space associated with these characteristics. Six models describing different sets of source properties were examined. Models 1-4 differ in source lifetimes and radiation beaming angles, but were all fixed to produce the roughly the same number of ionizing photons. More specifically, the tail-end spectral index of the SED in these models was set to $\alpha_s = 1.8$, as in the SED proposed by Madau, Haardt, & Rees (1999), while the minimum B-band luminosity at $z = 0$ was set to $L_{min,o} = 1.42 \times 10^9\ L_{B,\odot}$ based upon an estimate from the results of Cheng et al. (1985). For comparison, models 5 and 6, were specifically designed to the produce substantially less ionizing emissivity while retaining plausible values for α_s and $L_{min,o}$ (see Table 1). As expected, there is a sharp contrast between the results from the two groups. Specifically, the IGM in models 1-4 is ionized earlier and more thoroughly than in models 5 and 6, resulting in significantly lower mean opacities for the spectra (see Figure 3 and 11) at redshifts $z \sim 3$.

Based solely on the limited number of measured He II opacities from observed quasar

spectra, it appears that the ionizing emissivities in models 1-4 are too high, resulting in mean opacities lower than the observed values at all redshifts. If we accept our choice for M_{min} as being reasonable, then the SED and/or $L_{min,o}$ need to be adjusted in order to better match the observations. In model 5, we picked a value of for $L_{min,o}$ that was a factor of 4 times higher than the value in models 1-4. Although this seems like a large difference from the original estimate of Cheng et al. (1985), a quick glance at Figure 1 of their paper reassures us that such a choice for the limiting luminosity (magnitude) for quasars is still plausible if we assume that the LF of Seyfert galaxies is similar to the LF of quasars. The tail-end spectral indices in models 5 and 6 were set to $\alpha_s = 2.0$ and $\alpha_s = 2.3$ respectively, which also represent plausible choices given the range of indices derived from observations of the EUV spectra of radio-quiet quasars at intermediate redshifts (Zheng et al. 1998).

That model 5 provides the best match to observations of the mean optical depth bolsters the corresponding choices for α_s and $L_{min,o}$. However, as model 6 makes clear, varying α_s alone within a plausible range yields more than enough leeway to also match the observations while retaining the more widely quoted value for $L_{min,o}$ (see, e.g., Haardt & Madau 1996; Madau, Haardt, & Rees 1999; Bianchi et al. 2001). Furthermore, the results from model 3 suggest that the choice for source lifetimes may also affect the overall ionization state of the IGM, adding a further free parameter.

However, uncertainties in the clumping, because of small scale power, and the gas temperatures do not allow us to clearly eliminate specific models using existing observational data. Therefore, we refrain from discussing best fits to the observations since we clearly have not conducted a comprehensive study of the associated parameter space. Rather, the main purpose of this paper is to provide a basic overview on how source characteristics influence global properties of the reionization process.

Some specific insights from our analysis are as follows:

1. The systematic increase in the clumping factors associated with ionized regions towards low redshifts once most of the volume has already been ionized is consistent with the argument that in the post-reionization stage, the densest clouds and filaments become gradually ionized to higher degrees as the mean ionizing intensity increases.

2. The dispersion of the mean photoionization rates appears to be remarkably large and explicitly demonstrates the non-uniform nature of a radiation field dominated by local sources. Although dispersion levels do show signs of decreasing at the lowest redshifts when background intensities begin to exceed the intensities from local sources, the results demonstrate the importance of solving the radiation field locally during and before the epoch of reionization. The relatively large dispersion seen in models 2 and 3 can be

attributed to the large number of sources which can lead to highly irregular radiation fields.

3. Measurements of the number of intersections as function of transmittance and the TPDF of Lyα spectra offer insightful information regarding the ionization state of the IGM at specific times. In particular, both methods appear to be very sensitive to small differences in the underlying ionization fractions and as a result serve as useful tools to differentiate between spectra (models) that at first glance seem quite similar.

4. The lifetimes of the sources responsible for reionization may have an impact on the overall evolution of the process. Since sources tend to live in the densest regions of the IGM, the ionizing flux must first break through their dense surroundings in order to reach the IGM. Such an effect has been postulated for the spectrum of HS1700+6416 (Davidsen et al. 1996). One may therefore argue that the inability of model 3 to bring the IGM to high level of ionization relative to models 1, 2 and 4 might have to do with the fact that the relatively short lifetime requires a larger number of sources to be involved in reionization, effectively requiring more of the total ionizing flux to emanate from inside the densest structures. As a result, the IGM may be subject to less of the cumulative ionizing potential of the sources. One might wonder why model 2, which actually invokes even more sources than model 3 does not yield similar trends. In that case, the beaming of the radiation allows the sources to more easily "break out" of the dense absorbers which surround them thereby allowing more of the radiation to reach the diffuse IGM. The opposite case to model 3 occurs for model 4 where the longer lifetimes require fewer sources be invoked. In this case, by definition, there will be relatively fewer absorbers through which the sources have to shine their flux during the course of reionization. Consequently, the IGM in model 4 appears to be relatively more ionized than the other models.

Our analysis reflects a first step to model radiative transfer effects and to develop new insights into open questions regarding the reionization of the universe. In particular, the method used here can be modified to study the reionization of H I, offering further opportunities for comparisons with observations, especially in light of recent evidence for the reionization of H I at $z \sim 6$ (Becker et al. 2001). Furthermore, analysis of both H I and He II Lyα opacities from simulated spectra and observational results can constrain the contribution of starburst galaxies to the UV ionizing background (see, e.g., Bianchi et al. 2001; Kriss et al. 2001). We also envision supplementing our method to include the effect of heating from photoionization to explore the possibility of searching for fluctuations in the IGM temperature using the Lyα forest (see, e.g, Zaldarriaga 2001).

REFERENCES

Abel, T., Haehnelt, M. G. 1999, ApJ, 520, L13

Anderson, S. F., Hogan, C. J., Williams, B. F., & Carswell, R. F. 1999, AJ, 117, 56

Becker, R. H., Fan, X., White, R. L., Strauss, M. A., Narayanan, V. K., Lupton, R. H., Gunn, J. E., Annis, J., Bahcall, N. A., Connolly, A. J., Csabai, I., Czarapata, P. C., Doi, M., Heckman, T. M, Hennessy, G. S., Knapp, G. R., Lamb, D.Q., Nash, T., Nichol, R., McKay, T. A., Munn, J. A., Pier, J. R., Richards, G. T., Schneider, D. P., Stoughton, C., Szalay, A. S., Thakar, A. R. 2001, ApJ, in press (astro-ph/0108097)

Bianchi, S., Cristiani, S., Kim, T.S. 2001, A&A, in press (astro-ph/0106526)

Boyle, B. J., Shanks, T., & Peterson, B. A. 1988, MNRAS, 235, 935

Cen, R., Miralda-Escudé, J., Ostriker, J.P. & Rauch, M. 1994, ApJ, 427, L9

Cheng, F. Z., Danese, De Zotti, G., & Franceschinni, A. 1985, MNRAS, 212, 857

Cooke, A. J., Espey, B., & Carswell, R. F. 1997, MNRAS, 284, 552

Croft, R.A.C., Weinberg, D.H., Katz, N. & Hernquist, L. 1997, ApJ, 488, 532

Croft, R.A.C., Di Matteo, T., Davé, R., Hernquist, L., Katz, N., Fardal, M.A. & Weinberg, D.H. 2001, ApJ, 557, 67

Davé, R., Hernquist, L., Katz, N. & Weinberg, D.H. 1999, ApJ, 511, 521

Davé, R., Cen, R., Ostriker, J.P., Bryan, G.L., Hernquist, L., Katz, N., Weinberg, D.H., Norman, M.L., & O'Shea, B. 2001, ApJ, 552, 473

Davidsen, A. F., Kriss, G. A., & Zheng, W. 1996, Nature, 380, 47

Francis, P. J., Hewett, P. C., Foltz, C. B., Chaffee, F. H., Weymann, R. J., & Morris, S. L. 1991, ApJ, 373, 465

Giallongo, E., Cristiani, S. D'Odorico, S., Fontana, A., & Savaglio, S. 1996, ApJ, 466, 46

Gnedin, N.Y. 2000, ApJ, 535, 530

Haardt, F., & Madau, P. 1996, ApJ, 461, 20

Haiman, Z., & Loeb, A. 1998, ApJ, 503, 505

Harris, D. L. 1948, ApJ, 108, 112

Heap, S. R., Williger, G. M., Smette, A., Hubeny, I., Sahu, M. S., Jenkins, E. B., Tripp, T. M., Winkler, J. N. 2000, ApJ, 534, 69

Hernquist, L., Katz, N., Weinberg, D.H., & Miralda-Escudé, J. 1996, ApJ, 457, L51

Hogan, C. J., Anderson, S. F.., & Rugers, M. H. 1997, AJ, 113, 1495

Jakobsen, P. 1996, in Science with Hubble Space Telescope II, ed. P. Benvenuti, F. D. Macchetto, & E. J. Schreier (Baltimore: STScI), 153

Jakobsen, P., Boksenberg, A., Deharveng, J. M, Greenfield, P., Jedrzejewski, R., & Paresce, F. 1994, Nature, 370, 35

Katz, N., & Quinn., T. 1995, TIPSY manual

Katz, N., Weinberg, D.H. & Hernquist, L. 1996, ApJS, 105, 19

Kriss, G. A., Shull, J. M., Oegerle, W., Zheng, W., Davidsen, A. F., Songaila, A., Tumlinson, J., Cowie, L. L., Deharveng, J.-M., Friedman, S. D., Giroux, M. L., Green, R. F., Hutchings, J. B., Jenkins, E. B., Kruk, J. W., Moos, H. W., Morton, D. C., Sembach, K. R., Tripp, T. M. 2001, Science, 293, 5532

Machacek, M. E., Bryan, G. L., Meiksin, A., Anninos, P., Thayer, D., Norman, M., & Zhang, Y. 2000, ApJ, 532, 118

Madau, P., Haardt, F., Rees, M. J. 1999, ApJ, 514, 648

McDonald, P., Miralda-Escudé, J., Rauch, M., Sargent, W.L.W., Barlow, T.A., Cen, R., Ostriker, J.P. 2000, ApJ, 543, 1

Miralda-Escudé, J., Haehnelt, M., & Rees, M. J. 2000, ApJ, 530, 1

Miyaji, T., Hasinger, G., Schmidt, M. 2000, A&A, 353, 25

Peebles, P. J. E. 1993, Principals of Physical Cosmology (Princeton: Princeton Univ. Press)

Pei, Y. C. 1995, ApJ, 438, 623

Press, W. H., & Schechter, P. 1974, ApJ, 532, 679

Rauch, M., Miralda-Escudé, J., Sargent, W.L.W., Barlow, T.A., Weinberg, D.H., Hernquist, L., Katz, N., Cen, R. & Ostriker, J.P. 1997, ApJ, 489, 7

Reimers, D., Köhler, S., Wisotzki, L., Groote, D., Rodriguez-Pascal, P., Wamsteker, W. 1997, A&A, 327, 890

Sargent, W. L. W., Steidel, C. C., & Boksenberg, A. 1989, ApJS, 69, 703

Schmidt, M., Schneider, D. P., Gunn, J. E. 1995, AJ, 110, 68

Smette, A., Heap, S. R., Williger, G. M., Tripp, T. M., Jenkins, E. B., Songaila, A. 2000, ApJ, submitted (astro-ph/0012193)

Sokasian, A., Abel, T. & Hernquist, L. 2001, NewA, 6, 359 (Paper I)

Springel, V. & Hernquist, L. 2001, MNRAS, submitted [astro-ph/0111016]

Springel, V., Yoshida, N., White, S. D. M. 2001, NewA, 6, 795 (astro-ph/0003162)

Springel, V., White, M. & Hernquist, L. 2001, ApJ, 549, 681 [astro-ph/0008133]

Tytler, D. 1995, in QSO Absorption Lines, Proc. ESO Workshop (G. Meylan ed.), Springer, Berlin, p.289

Warren, S.J., Hewett, P.C., & Osmer, P.S. 1994, ApJ, 421, 412

Zaldarriaga, M. 2001, ApJ, submitted (astro-ph/0102205)

Zhang, Y., Anninos, P. & Norman, M.L. 1995, ApJ, 453, L57

Zheng, W., Kriss, G. A., Telfer, R. C., Crimes, J. P., & Davidsen, A.F. 1998, ApJ, 492, 855

TABLE 1

Source Parameters

Model	T_{life} [10^7 yrs]	$L_{min,o}$ [$10^9 L_{B,\odot}$]	M_{min} [$10^{10} M_{\odot}$]	β [radians]	α_s
1	2.0	6.44	1.42	π	1.8
2	2.0	6.44	1.42	$\pi/2$	1.8
3	1.0	6.44	1.42	π	1.8
4	4.0	6.44	1.42	π	1.8
5	2.0	25.8	1.42	π	2.0
6	2.0	6.44	1.42	π	2.3

Fig. 1.— The number of He II ionizing photons per unit comoving volume released from the sources as a function of redshift in each of the six models. The solid histogram in each plot specifies the number of ionizing photons released per unit volume in each redshift bin and the corresponding dashed curve represents the cumulative value. The widths of the bins in each histogram represent the associated source lifetimes. The total number of sources invoked is noted in the upper right of each plot (see text for discussion).
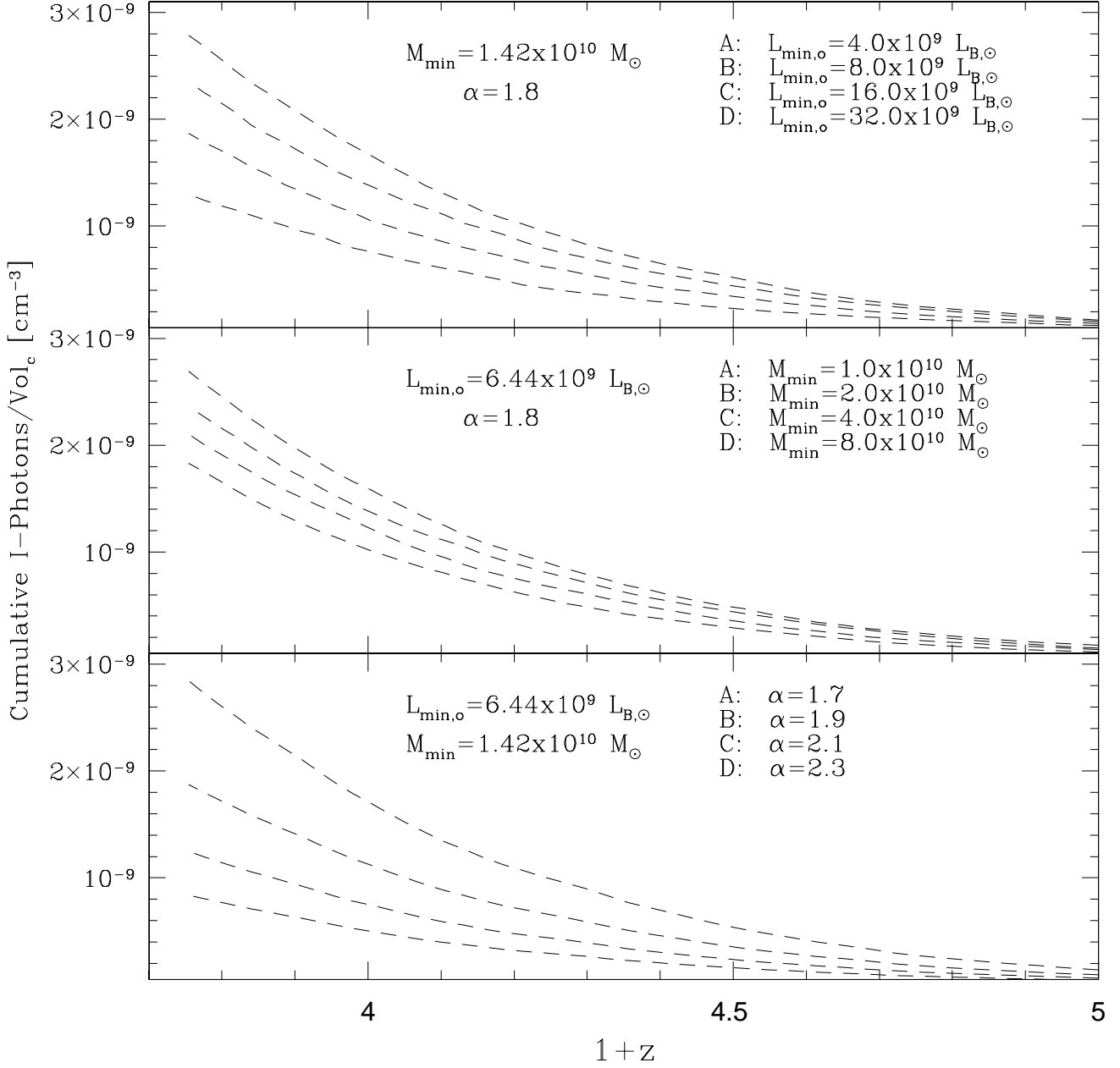
Fig. 2.— Cumulative number of ionizing photons that are released per unit comoving volume as a function of redshift in our analysis as we vary the parameters M_{min}, $L_{min,o}$, and α_s separately (see text for definitions). Labels A, B, C, and D refer to the curves in each plot in a top-down respective order.
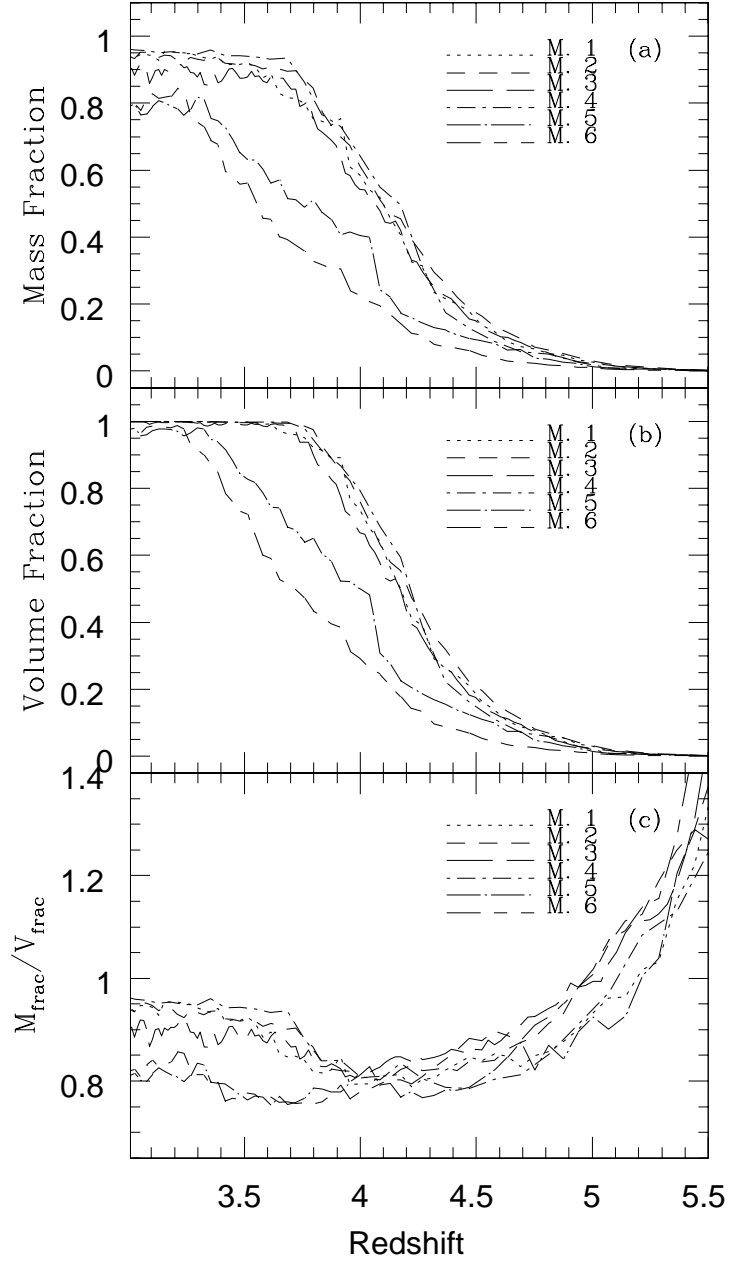
Fig. 3.— Evolution of the ionized mass fraction (a), ionized volume fraction (b), and the ionized mass to volume ratio (c) as functions of redshift for each model. In each case, full volume ionization of the Helium II is essentially attained by a redshift $z \simeq 3.3$ with the volume fraction being consistently larger than the mass fraction for $z \lesssim 5$ (see text for discussion).
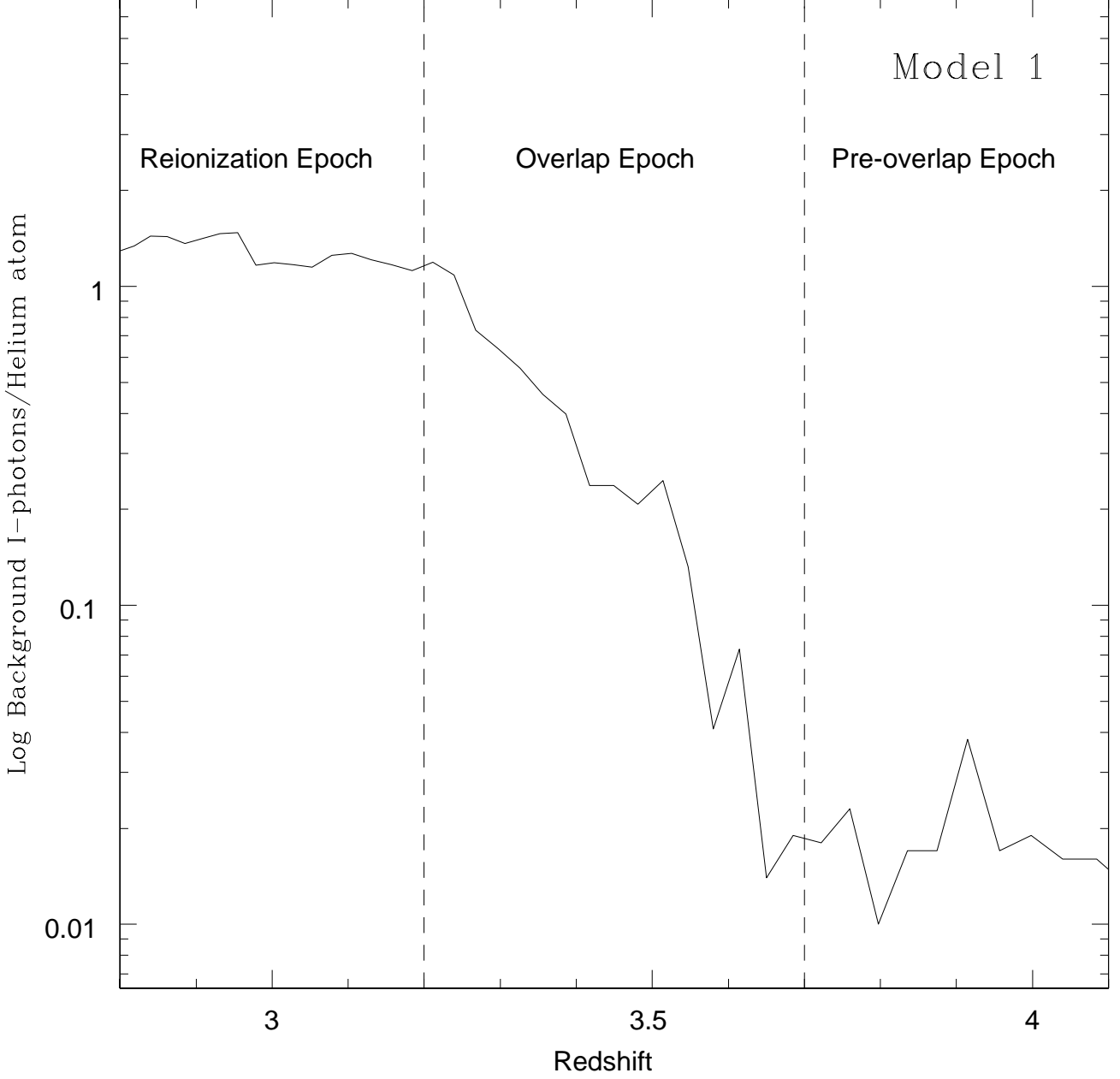
Fig. 4.— Evolution in the number of ionizing photons per helium atom available in the diffuse background component of the radiation field. The region between the vertical dashed lines represents a short fraction of a Hubble time where the intensity dramatically increases, characteristic of an overlap epoch (e.g. Gnedin 2000).
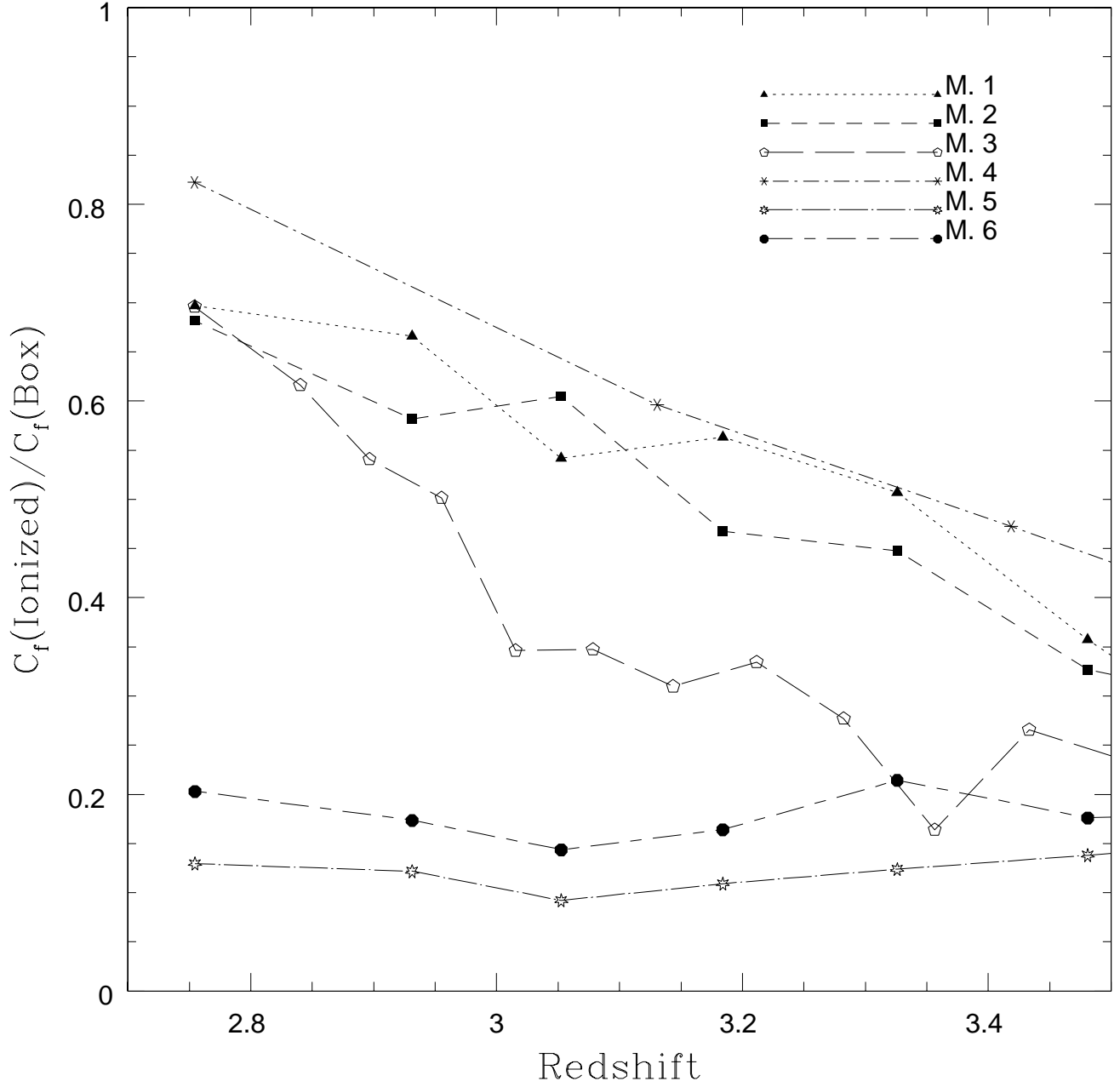
Fig. 5.— Evolution of the ratio of the clumping factor within regions that have been highly ($> 90\%$) ionized in mass to the ratio of the clumping factor of the entire volume. The low levels for model 5 and 6 reflect their inability to keep the densest cells ionized. The general uptrend towards lower redshifts seen in the other models is consistent with ionization zones expanding into the densest structure harboring relatively more clumped gas.
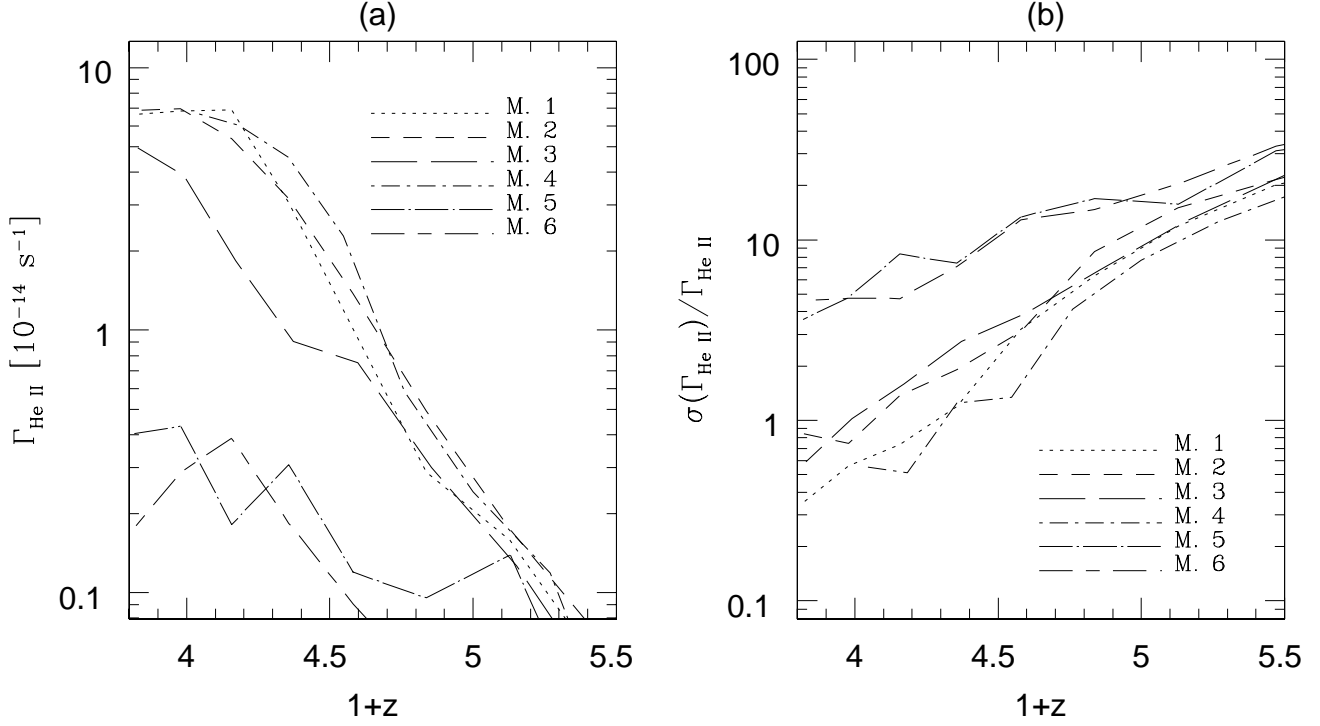
Fig. 6.— Evolution of the mean volume-weighted photoionization rate in the simulation volume (*left*) and corresponding dispersion ratio (*right*) for each model. Mean rates were obtained by averaging over all cells in the grid.
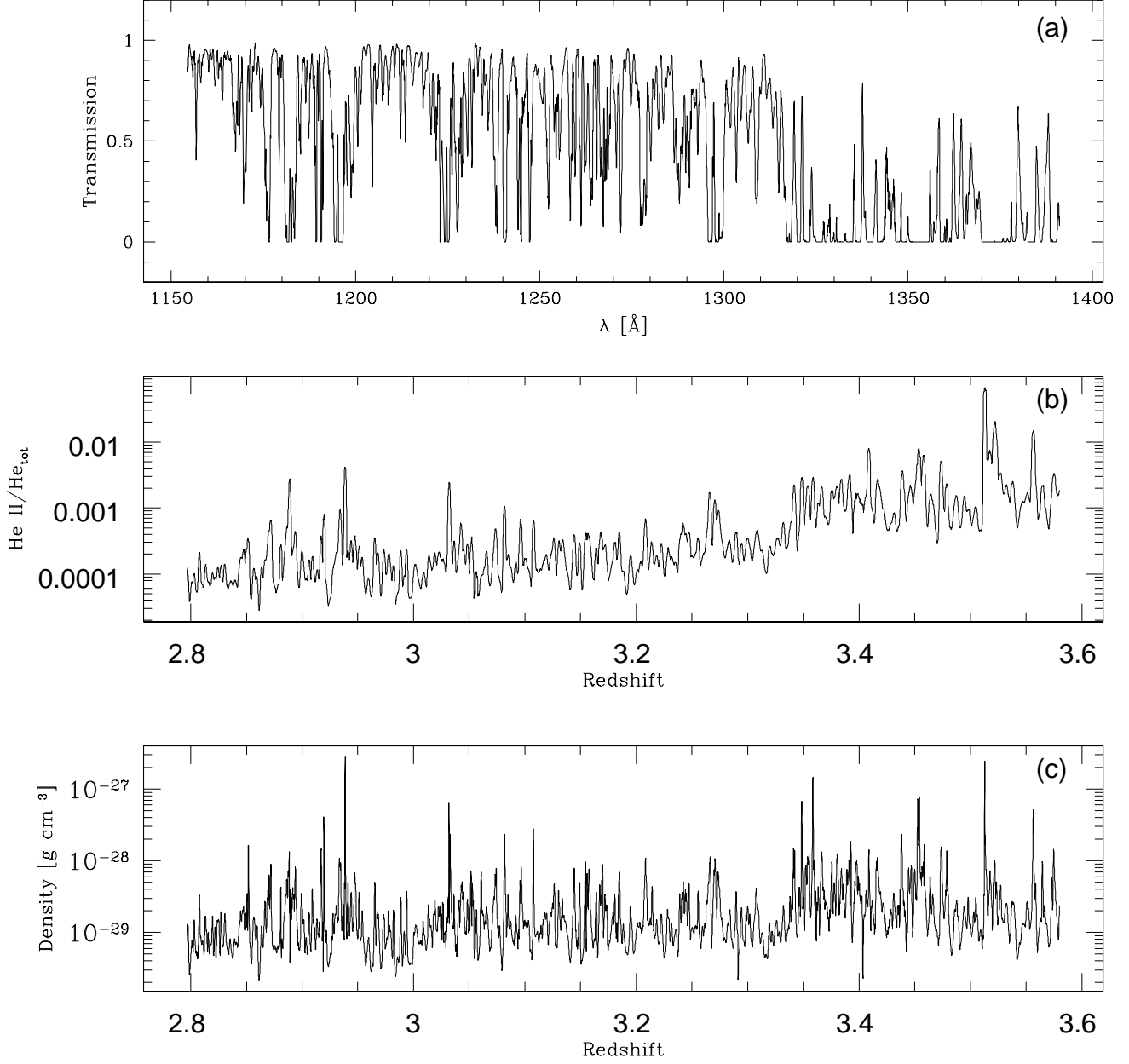
Fig. 7.— Sample transmission spectrum (a) from model 1 spanning λ =1150-1400 Å along with the corresponding HeII fraction (b) and gas density (c) along the LOS out to z =3.6.
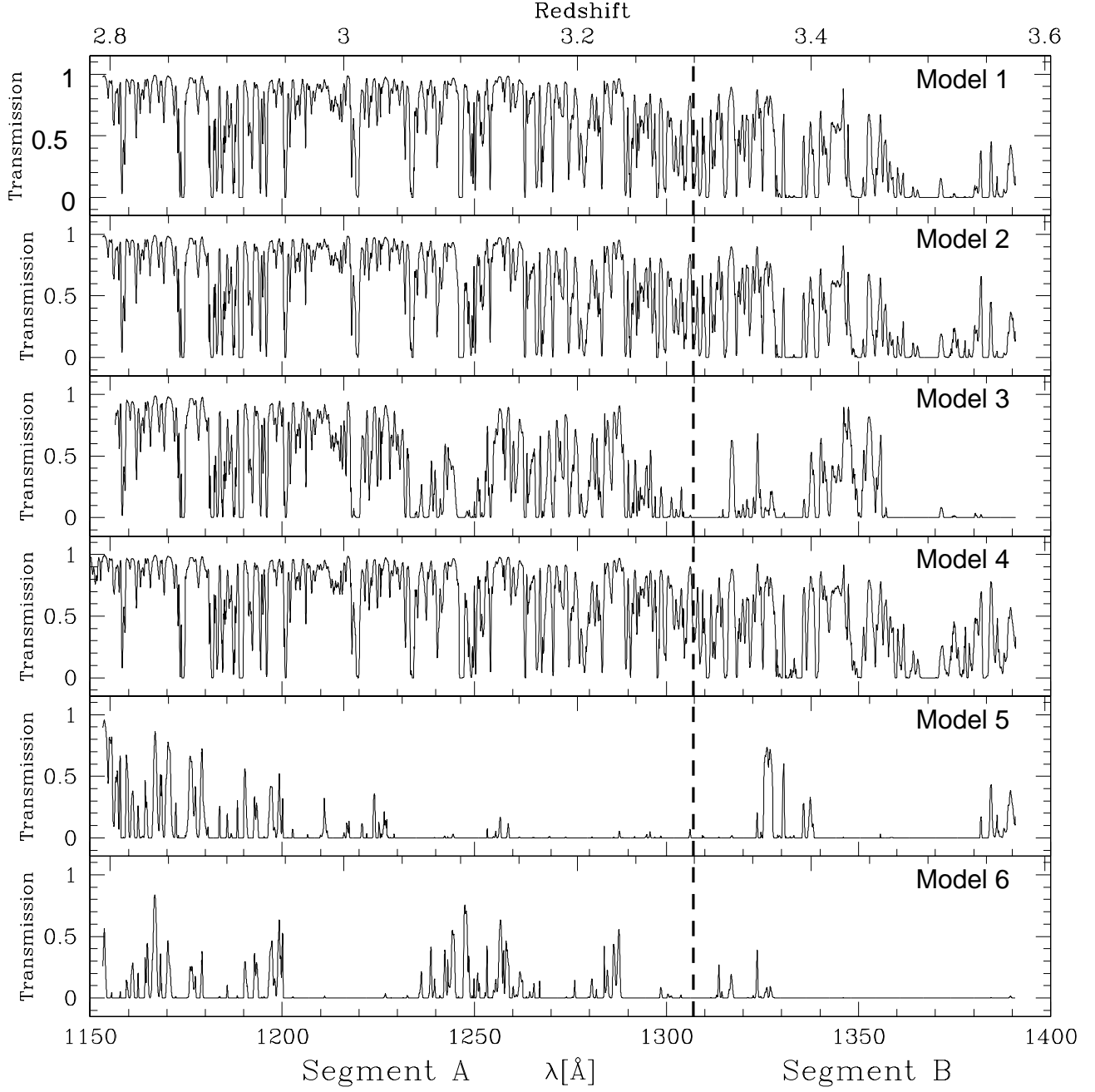
Fig. 8.— Transmission spectra along a particular LOS out to $z = 3.6$ extracted from the six models. The dashed vertical line delineates where the spectra were divided for analysis purposes.
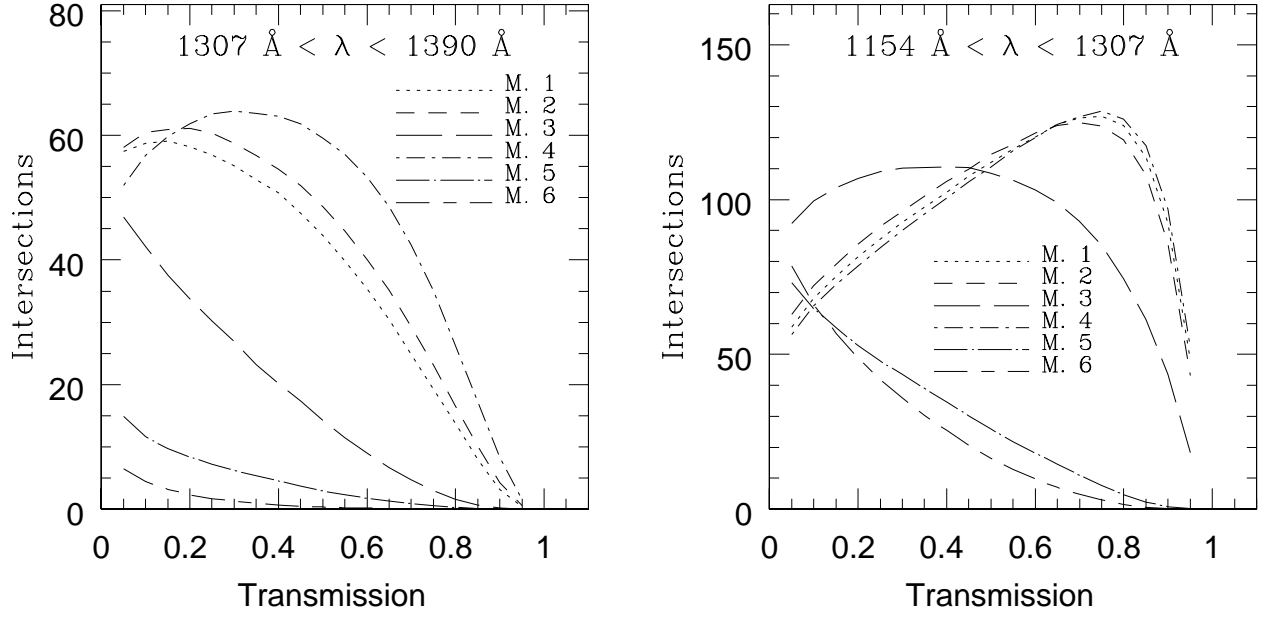
Fig. 9.— Number of intersections through segment B (*left*) and segment A (*right*) of the spectra of each model as a function of transmission. Note the strong contrast between models within each regime and the evolution of the curves between the regimes.
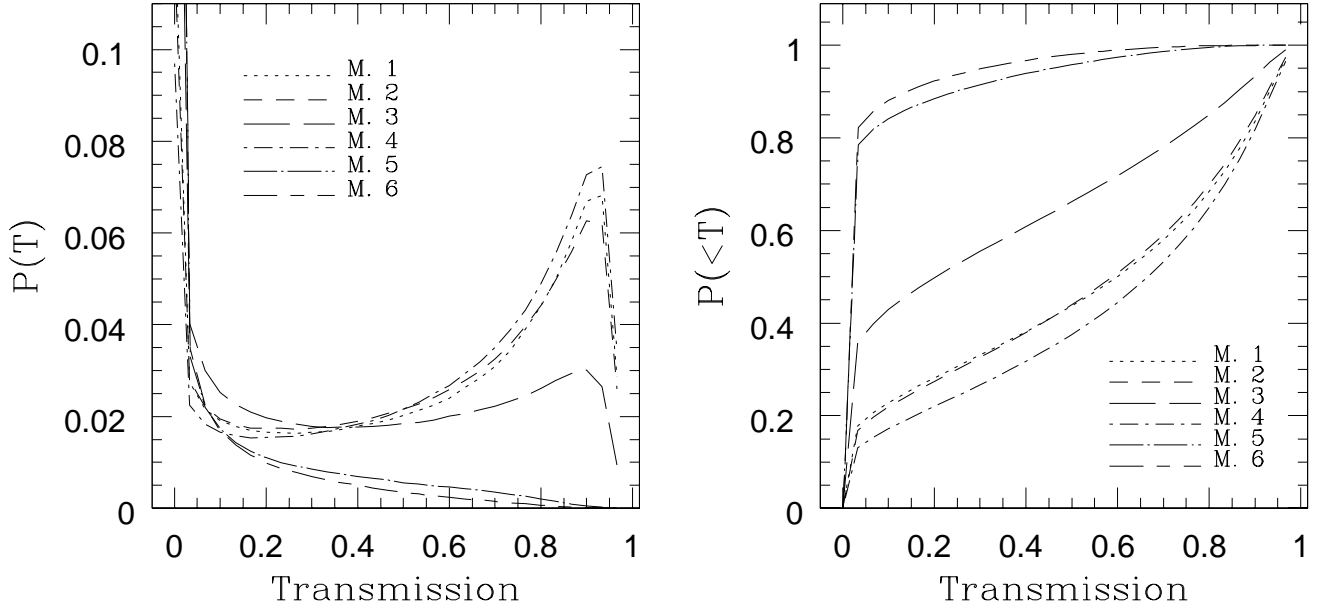
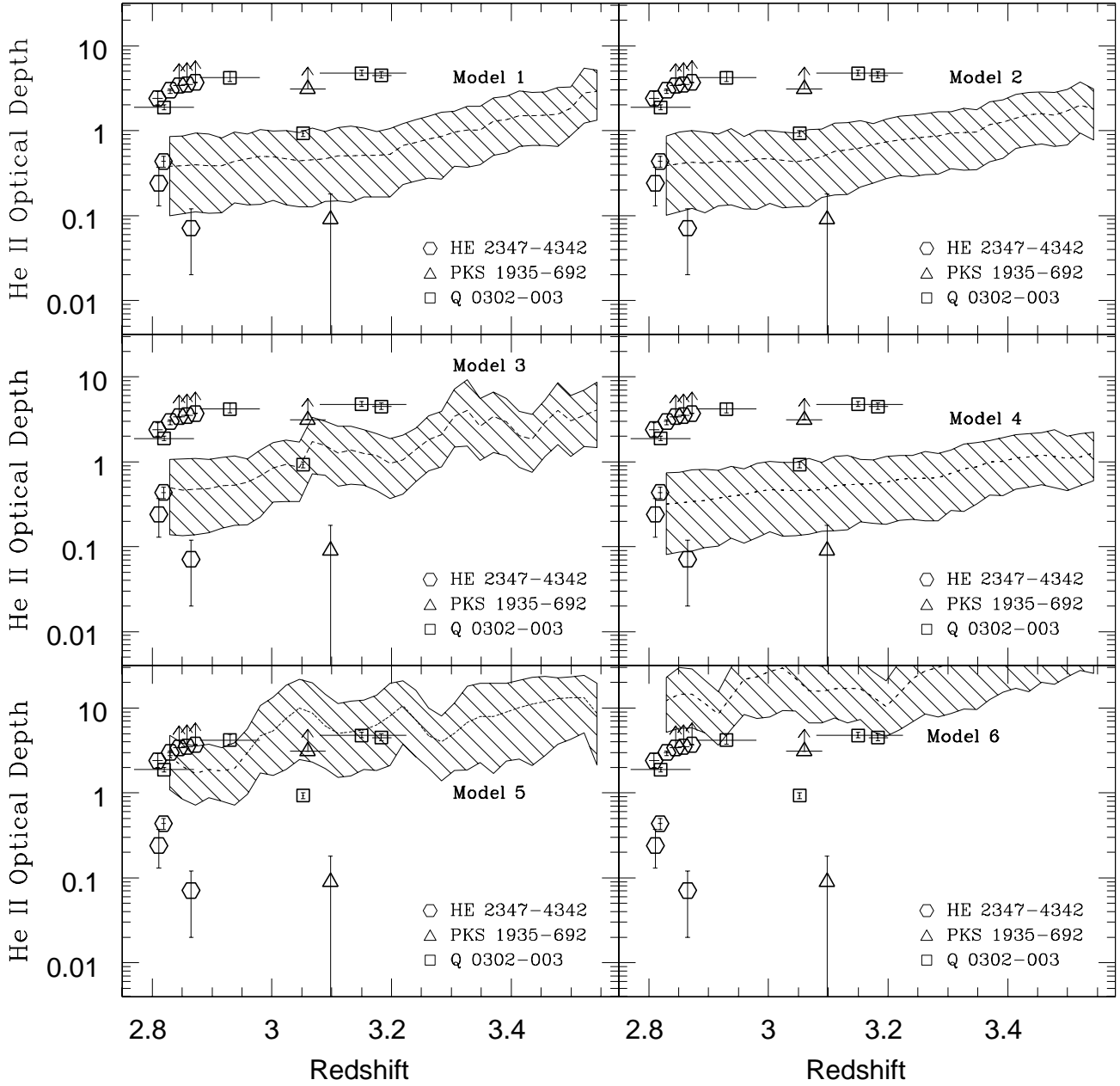Fig. 10.— TPDF (*left*) and the cumulative TPDF (*right*) for each of the models averaged over 500 spectra.

Fig. 11.— Redshift evolution of the effective mean optical depth of He II absorption. Hatched regions represent the optical depth derived from the simulations at the 95% confidence level with the dashed lines indicating mean values. Observational results from quasars HE 2347-4342, PKS 1935-692 and Q 0302-003 are plotted for comparison.
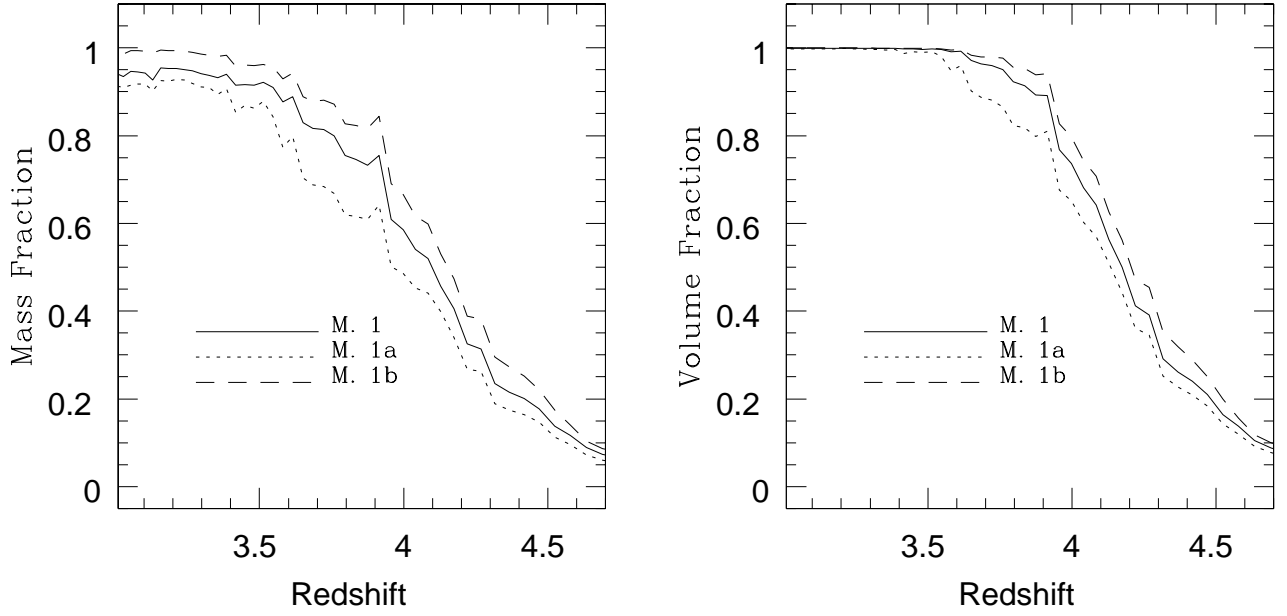
Fig. 12.— Comparison of the ionized mass fraction (*left*) and ionized volume fraction (*right*) as a function of redshift between models 1, 1a, and 1b. Models 1a and 1b are identical to model 1 except for the ionized gas temperatures and clumping factors, respectively. In model 1a the ionized gas temperature was set to 7000 K and in model 1b, clumping factors were all set to unity.
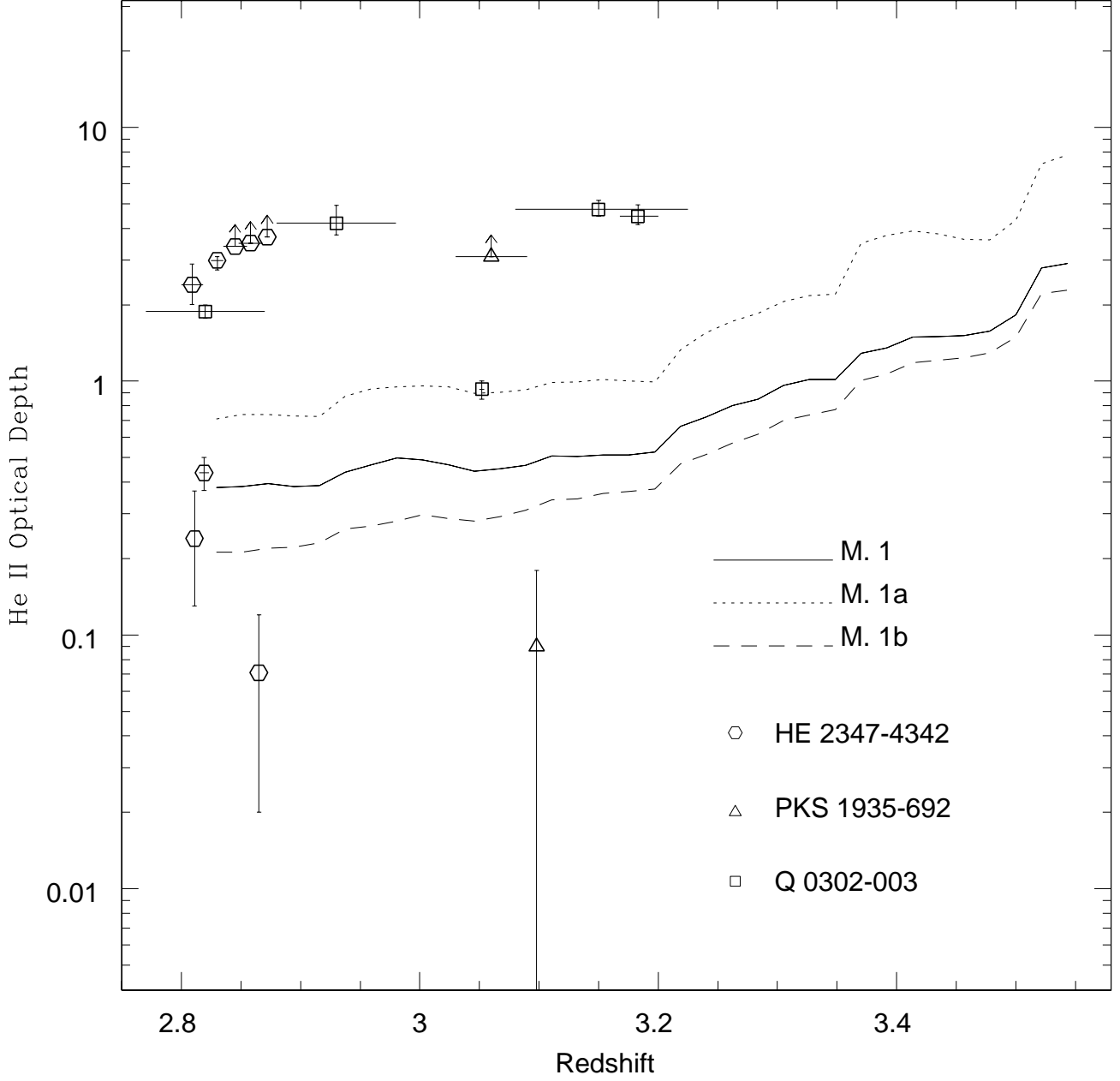
Fig. 13.— Comparison of the redshift evolution of the effective mean optical depth of He II absorption between models 1, 1a and 1b.